IEEE Access
Multidisciplinary | Rapid Review | Open Access Journal

Received 17 May 2024, accepted 31 May 2024, date of publication 6 June 2024, date of current version 17 June 2024.

*Digital Object Identifier 10.1109/ACCESS.2024.3410326*

RESEARCH ARTICLE

# Thermal Modeling and Analysis of a HPMSM Coupling With Magnetic Bearings

**LIU BIN, YU ZHONGJUN, AND FU JIA**
National Key Laboratory of Electromagnetic Energy, Naval University of Engineering, Wuhan 430033, China
Corresponding author: Fu Jia (fujia8@mail.ustc.edu.cn)

This work was supported in part by the National Natural Science Foundation of China under Grant 52077217; and in part by the National Key Laboratory of Electromagnetic Energy, Naval University of Engineering.

**ABSTRACT** The supercritical $CO_2$ Brayton cycle (S-$CO_2$ BC) has attracted increasing attention because of the advantages of high efficiency, better compatibility, and safety, and to further improve the power density, turbine alternator compressor (TAC) integrated high-speed permanent magnet synchronous machine (HPMSM) sets are usually used in S-$CO_2$ BC power generation devices. In terms of safe operation, it is of great significance to accurately and quickly obtain the temperature in the coupling state of the machine and magnetic bearings. Taking a 40000rpm HPMSM set used in S-$CO_2$ BC power generation devices as an example, a new equivalent thermal model of winding is proposed firstly, and the temperature difference between the equivalent model and the exact model is less than 1.7%. On this basis, the lumped parameter thermal network (LPTN) model of the HPMSM set under the coupling state of the machine and magnetic bearings in totally enclosed environment is established. Finally, the steady and transient temperature results of the HPMSM set are obtained, which are verified by computational fluid dynamics (CFD) method. The range of absolute temperature error between LPTN model and CFD model is 0.2°C∼2.2°C in steady state, and the relative temperature error is less than 4.2% in transient state. Furthermore, the computational efficiency of LPTN model is greatly improved compared with CFD model. The research of this paper is of great significance to temperature analysis and prediction under the coupling state of machine and magnetic bearings.

**INDEX TERMS** HPMSM, magnetic bearings, thermal analysis, LPTN.

## I. INTRODUCTION

Due to environmental pollution and energy shortages, renewable and sustainable energy sources are gradually replacing traditional fossil fuels, and higher energy efficiency has become the most concerning issue for researchers [1], [2]. The S-$CO_2$ BC has attracted increasing attention because of its high thermal cycling efficiency, better compatibility with structural materials, better safety and reliability, which has been successfully applied in fields such as nuclear power plants and solar power tower plants [3], [4]. As a trend, energy conservation and emission reduction have also become key issues that urgently need to be addressed in the field of shipbuilding. Considering the enormous potential of S-$CO_2$ BC technology in improving ship fuel utilization, high-temperature flue gas waste heat utilization, and energy conservation [5], [6], its application in ship power generation units is becoming an emerging research hotspot.

In order to improve the power density of the generator and achieve a highly compact cycle structure, small diameter and high-speed turbine alternator compressor (TAC) integrated HPMSM set is usually used in S-$CO_2$ BC power generation devices [5], [7], [8]. Nevertheless, the high-speed characteristic has brought new problems. On the one hand, the significantly increasing rotor speed results in higher mechanical friction losses [9], [10], [11]. To reduce these losses and control the vibration and noise, magnetic bearings are commonly used instead of mechanical bearings. Meanwhile, extra losses are also introduced from magnetic bearings, which have to be considered when conducting thermal analysis and

The associate editor coordinating the review of this manuscript and approving it for publication was Kai-Da Xu.

© 2024 The Authors. This work is licensed under a Creative Commons Attribution-NonCommercial-NoDerivatives 4.0 License.
For more information, see https://creativecommons.org/licenses/by-nc-nd/4.0/

cooling design [12], [13], [14]. On the other hand, due to the smaller size and higher compactness of high-speed machine, the heat source is more concentrated in space, which is not conducive to heat dissipation [15]. It can cause critical components, such as windings, to overheat, and lead to insulation aging when the machine is under long-term operation [16], which would affect the normal operation of the HPMSM set.

The above issues pose higher requirements for the cooling design of high-speed machine coupling with magnetic bearings. Besides, accurate acquisition of the temperature characteristics is the premise of cooling design. There are three main methods for analyzing temperature characteristics: FEM (finite element method), CFD (computational fluid dynamics), and LPTN (lumped parameter thermal network). The advantage of FEM and CFD is that they have high accuracy and can obtain more detailed temperature characteristics, but the cost of computation is huge [17], [18]. Therefore, LPTN is often preferred thanks to their lower computational effort along with good accuracy [19], [20]. Furthermore, CFD and FEM are more commonly used to analyze steady temperature characteristics, in situations where rapid acquisition of transient temperature or real-time monitoring of temperature is required, LPTN is more widely used due to its high computational efficiency and good computational accuracy [21], [22].

However, the current research about LPTN model of HPMSM coupling with magnetic bearings still needs to be enriched. At first, there are few studies on the equivalent thermal model of key components such as stator winding [23], [24]. Then, most of the existing research established the LPTN model based on classical mode [19], [20] [27], [28], [29], but according to theoretical derivation, the T model should be used for components with loss to obtain more accurate temperature results [22], [25]. In addition, there are few studies on LPTN model and thermal analysis under the coupling state of HPMSM and magnetic bearings. Therefore, to ensure the safe operation of the HPMSM set and guide cooling design, it is necessary to establish a fast and accurate temperature analysis model by using LPTN method under the coupling state of HPMSM and magnetic bearings.

In this paper, taking a HPMSM set used in S-$CO_2$ BC power generation devices as an example, the thermal model based on LPTN with high computational efficiency and good accuracy is established, and the thermal characteristics are analyzed. Firstly, the key parameters of the HPMSM and magnetic bearings are introduced, along with the losses. Then, the equivalent thermal model of stator winding is proposed through theoretical analysis, and verified by FEM and experiment. Finally, the thermal model based on LPTN is established under the coupling state of the HPMSM and magnetic bearings, and the temperature results in both steady and transient states are obtained and verified by CFD. The study in this paper is of great significance to temperature analysis and prediction under the coupling state of HPMSM and magnetic bearings

## II. MODEL ANALYSIS AND LOSS CALCULATION

### A. KEY PARAMETERS OF THE HPMSM SET

The HPMSM set for S-$CO_2$ BC power generation devices is composed of front radial magnetic bearing (RMB), HPMSM, rear radial magnetic bearing, and axial magnetic bearing (AMB). The specific configuration is shown in FIGURE 1

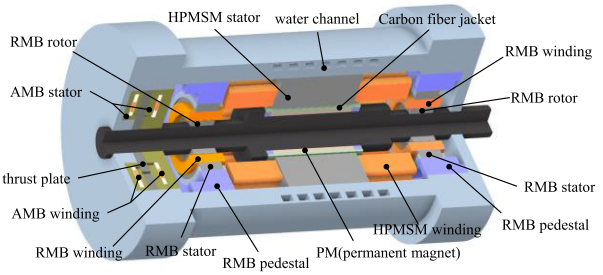


**FIGURE 1. Configuration of the HPMSM set.**

The key parameters of RMB and AMB are shown in TABLE 1. The RMB adopts the 8-pole topological structure, and the AMB adopts the conventional C-type structure. The current stiffness and displacement stiffness are shown in TABLE 2, and the mechanical characteristics of the major materials of RMB and AMB are shown in TABLE 3. The cross-section diagrams of RMB and AMB are shown in FIGURE 2.

**TABLE 1. Key parameters of RMB and AMB.**

| Parameters | Symbols | Values | Unit |
|---|---|---|---|
| RMB stator outside diameter | $R_{Rs2}$ | 80 | mm |
| RMB rotor outside diameter | $R_{Rr}$ | 40 | mm |
| RMB airgap length | $\delta_R$ | 0.6 | mm |
| shaft outside diameter | $R_{shaft}$ | 27.5 | mm |
| AMB stator inside diameter | $R_{As1}$ | 51.8 | mm |
| AMB stator outside diameter | $R_{As2}$ | 110 | mm |
| AMB thrust plate diameter | $R_{Ar}$ | 75 | mm |
| AMB airgap length | $\delta_A$ | 0.5 | mm |

**TABLE 2. Current stiffness and displacement stiffness of magnetic bearings.**

| Components | Current Stiffness/(N/A) | Displacement Stiffness/(N/mm) |
|---|---|---|
| RMB | 395 | 28536 |
| AMB | 2111 | 12960 |

**TABLE 3. Mechanical characteristics of materials.**

| Components | Material | Elastic Modulus/GPa |
|---|---|---|
| RMB stator & rotor | 20WTG1500 | 200 |
| AMB stator | No.10 Steel | 205 |
| AMB thrust plate | 25Cr2Ni4Mov | 206 |

The rated speed of the HPMSM is 40000rpm. The surfaces of the rotor magnets are wound by carbon fiber, and the winding is wound by litz wires. In order to restrain the high

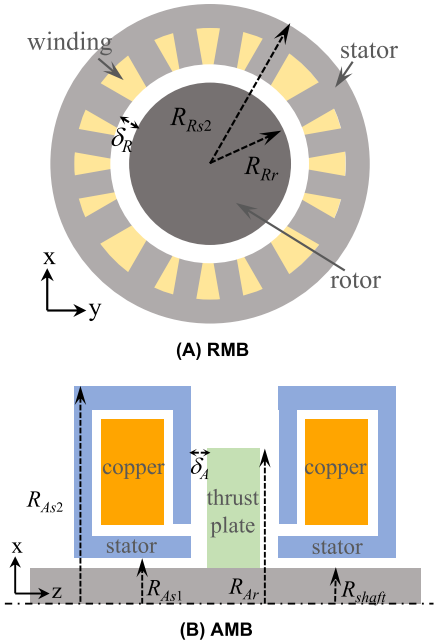


**FIGURE 2.** Cross-section diagrams of RMB and AMB.

frequency copper loss, especially the circulation copper loss, the coil transposition is adopted. The HPMSM adopts natural air cooling and water cooling, and the cooling waterway is provided in the housing. FIGURE 3 presents the cross-section diagram of the HPMSM, and its key parameters are shown in TABLE 4.

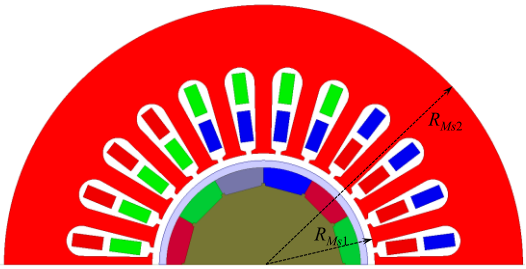


**FIGURE 3.** Cross-section diagram of the HPMSM.

**TABLE 4.** Key parameters of the HPMSM.

| Parameters | Symbols | Values | Unit |
|---|---|---|---|
| stator outer radius | $R_{Ms2}$ | 130 | mm |
| stator inner radius | $R_{Ms1}$ | 58 | mm |
| airgap length | $\delta_M$ | 3.5 | mm |
| stack length | $l_a$ | 150 | mm |
| stator slot number | $N_s$ | 24 | -- |
| rotor pole pair number | $p$ | 1 | -- |
| rated rotational speed | $N$ | 40000 | rpm |

Major materials and their thermal properties are listed in TABLE 5, where $c_p$ is specific thermal capacity [J/(kg·K)], $\rho$ is density [kg/m$^3$], and $\lambda$ is thermal conductivity [W/(m·K)]. It is a remarkable fact that the thermal conductivity of the HPMSM stator and RMB stator and rotor is anisotropic, and the suffixes r, c, and a represent the radial, circumferential, and axial thermal conductivities respectively.

**TABLE 5.** Material properties.

| Components | Material | $c_p$ | $\rho$ | $\lambda$ |
|---|---|---|---|---|
| | | J/(kg·K) | kg/m$^3$ | W/(m·K) |
| housing | Aluminum | 871 | 2660 | 162 |
| HPMSM stator | 20WTG1500 | 460 | 7650 | 26(r)26(r)2(a) |
| HPMSM rotor | 25Cr2Ni4Mov | 460 | 7800 | 45 |
| RMB stator & rotor | 20WTG1500 | 460 | 7650 | 26(r)26(c)2(a) |
| AMB stator | No.10 steel | 470 | 7900 | 40 |
| winding | Copper | 389 | 8950 | 398 |
| PM | SmCo32H | 335 | 8400 | 12 |

### B. LOSS CALCULATION

As the heat sources in thermal analysis, the accurate calculation of loss is of great significance. In this section, the loss of the HPMSM and magnetic bearings under rated operation is analyzed by both FEM and analytical methods.

#### 1) COPPER LOSS

The rated speed of the analyzed HPMSM set is 40000rpm, which corresponds to a fundamental frequency of 666.7Hz for armature currents where the pole pair number of the machine is 1. In addition, the diameter of the conductors is 1mm, thus besides the direct current (DC) copper loss, the circulation copper loss and eddy copper loss also should be considered, which could be obtained by FEM.

#### 2) CORE LOSS

According to the Bertotti core loss model [26], the core loss $P_{core}$ could be expressed as:

$$P_{core} = k_h f B_m^{\beta} + k_c f^2 B_m^2 + k_e f^{1.5} B_m^{1.5} \tag{1}$$

where, $k_h$, $k_c$, and $k_e$ are the coefficient of hysteresis loss, eddy current loss, and excess loss respectively, $f$ is the fundamental alternating current magnetization frequency [Hz], and $B_m$ is the amplitude of the magnetic flux-density [T].

The $k_h$, $k_c$, and $k_e$ could be obtained by curve fitting using the least squares method based on the core loss characteristics of the silicon steel(20WTG1500), which is shown in TABLE 6.

**TABLE 6.** Core loss coefficients of stator silicon steel sheet.

| $k_h$/W·m$^{-3}$·T$^{-2}$s | $k_c$/W·m$^{-3}$·T$^{-2}$s$^2$ | $k_e$/W • m$^{-3}$ • T$^{-1.5}$s$^{1.5}$ |
|---|---|---|
| 151.39 | 0.22 | 2.07 |

#### 3) PM EDDY CURRENT LOSS

The eddy current loss in the rotor PM caused by the harmonics in air gap field yields in an alternating magnetization

period is [27]:

$$P_e = \frac{\int_{Te} \sum_{i=1}^{k} J_e^2 \Delta_e \sigma_r^{-1} l_a dt}{T_e} \tag{2}$$

where $P_e$ is the rotor PM eddy current loss[W], $J_e$ is the current density in each element[A/m$^2$], $\Delta_e$ is the element area[m$^2$], $l_a$ is the rotor axial length[m], $\sigma_r$ is the conductivity of the eddy current zone[S/m], and $T_e$ is the time corresponding to an alternating magnetization period in each element.

#### 4) AIR FRICTION LOSS

The air friction loss of the HPMSM set can be divided into two parts. The first part of air friction loss occurs in the air gap of the HPMSM and RMB, which could be calculated by the following equation [28]:

$$\begin{aligned} P_{air} &= kC_f \pi \rho_{air} \omega^3 r^4 l_a \\ C_f &= 0.515 \frac{(\delta/r)^{0.3}}{\mathrm{Re}_\delta^{0.5}}, \quad (500 < \mathrm{Re}_\delta < 10^4) \\ C_f &= 0.0325 \frac{(\delta/r)^{0.3}}{\mathrm{Re}_\delta^{0.2}}, \quad (10^4 < \mathrm{Re}_\delta) \\ \mathrm{Re}_\delta &= \frac{\rho_{air} \omega r \delta}{\mu_{air}} \end{aligned} \tag{3}$$

where $k$ is the rotor surface roughness coefficient, $C_f$ is the air friction coefficient, $\mathrm{Re}_\delta$ is the Reynold number, $\rho_{air}$ is air density[kg/m$^3$], $\omega$ is rotation angular velocity of rotor[rad/s], $r$ is the rotor outer radius[m], $l_a$ is the axial length of rotor[m].

The other part of air friction loss occurs in the air gap between thrust plate and stator in AMB, which could be calculated by the following equation [14]:

$$\begin{aligned} P_{air} &= 0.5 C_f \rho_{air} \omega^3 (r_2^5 - r_1^5) \\ C_f &= \frac{64}{3\mathrm{Re}_r}, \quad (\mathrm{Re}_r < 30) \\ C_f &= \frac{3.87}{\mathrm{Re}_r^{0.5}}, \quad (30 < \mathrm{Re}_r < 3 \times 10^5) \\ C_f &= \frac{0.146}{\mathrm{Re}_r^{0.2}}, \quad (3 \times 10^5 < \mathrm{Re}_r) \\ \mathrm{Re}_r &= \frac{\rho \omega r^2}{\mu_{air}} \end{aligned} \tag{4}$$

where $r_1$ and $r_2$ are the inner radius and outer radius of the rotor respectively[m], $\mathrm{Re}_r$ is the Reynold number.

In summary, the loss of the HPMSM and magnetic bearings is given in TABLE 7.

**TABLE 7. Loss of the HPMSM and magnetic bearings.**

| Components | Loss | Value/W |
|---|---|---|
| RMB | copper loss | 34.1 |
| | core loss of stator | 3.7 |
| | core loss of rotor | 129.7 |
| | air friction loss | 99.5 |
| HPMSM | copper loss | 1217 |
| | core loss of stator | 3690 |
| | PM eddy current loss | 160 |
| AMB | air friction loss | 1063 |
| | copper loss | 14.7 |
| | air friction loss | 36.8 |

## III. THERMAL MODELLING OF LPTN

### A. WINDING EQUIVALENT THERMAL MODEL

#### 1) SLOT-IN WINDING EQUIVALENT THERMAL MODEL

As one of the most important components, the heat dissipation of stator winding is directly related to the safe operation of the machine. However, modeling the actual stator winding is not only difficult but also greatly increases the amount of computation. Therefore, the equivalent thermal model of stator winding is important to analyze the temperature quickly and accurately.

As to the HPMSM set in this paper, the RMB and HPMSM adopt scatter winding, which means that the copper wires can be regarded as uniformly arranged in the slot. Thus, the stator winding of RMB is selected to establish the equivalent thermal model. Besides the copper wires, there is epoxy resin, impregnating varnish, wire enamel, slot wedge, and insulation paper in the slot, which could be treated as equivalent insulation layer here. An equivalent thermal model is proposed in FIGURE 4.

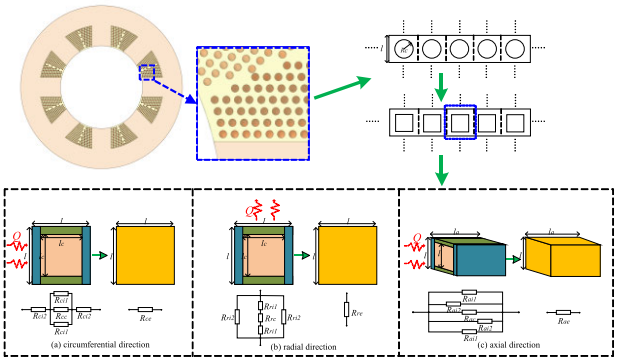


**FIGURE 4. Equivalent thermal model of slot-in winding.**

As is shown in FIGURE 4, the stator winding could be divided into many units, every single unit is composed of a copper wire and the equivalent insulation layer around it. The circular wire is equivalent to a square based on the conservation of volume:

$$l_c = \sqrt{\pi R_c^2}; \quad l = \sqrt{\frac{\pi R_c^2}{S_f}} \tag{5}$$

where $R_c$ is the diameter of the bare copper wire[m], $S_f$ is the bare wire fill factor, which could be obtained by $S_f = N\pi R_c^2/S_s$, $N$ is the number of copper wires, and $S_s$ is the area of slot[m$^2$].

Assuming that the heat transfer in radial, circumferential, and axial directions is independent of each other, so a single heat conduction unit in the slot can be decomposed into the structure shown in FIGURE 4 (a), (b), and (c), and the thermal

conductivity of the equivalent insulation layer is 0.2W/(m·K) according to [29].

The equivalent thermal conductivity of a single heat conduction unit in the circumferential direction could be derived as:

$$\begin{aligned} R_{ci1} &= \frac{l_c}{0.5(l-l_c)l_a\lambda_i} \\ R_{ci2} &= \frac{0.5(l-l_c)}{l_a l\lambda_i} \\ R_c &= \frac{l_c}{l_c l_a \lambda_c} \\ R_{ce} &= 2R_{ci2} + \frac{1}{\frac{1}{R_{ci1}} + \frac{1}{R_{ci1}} + \frac{1}{R_{cc}}} \\ &= \frac{(1+S_f-\sqrt{S_f})\lambda_i + (\sqrt{S_f}-S_f)\lambda_c}{l_a\lambda_i\left[(1-\sqrt{S_f})\lambda_i + \sqrt{S_f}\lambda_c\right]} \end{aligned} \tag{6,7}$$

$$\lambda_{ce} = \frac{l}{l_a l R_{ce}} = \frac{\lambda_i\left[(1-\sqrt{S_f})\lambda_i + \sqrt{S_f}\lambda_c\right]}{(1+S_f-\sqrt{S_f})\lambda_i + (\sqrt{S_f}-S_f)\lambda_c} \tag{8}$$

where $\lambda_c$ and $\lambda_i$ are the thermal conductivity of copper and equivalent insulation layer respectively[W/(m·K)]. Given $\lambda_c \gg \lambda_i$, the equation (7) could be simplified as the following:

$$\lambda_{ce} \approx \frac{\lambda_i}{1-\sqrt{S_f}} \tag{9}$$

Similarly, the equivalent thermal conductivity of a single heat conduction unit in radial and axial direction can be obtained as follows:

$$\begin{aligned} R_{ri1} &= \frac{0.5(l-l_c)}{l_c l_a \lambda_i} \\ R_{ri2} &= \frac{l}{0.5(l-l_c)l_a\lambda_i} \\ R_{rc} &= \frac{l_c}{l_c l_a \lambda_c} \\ R_{re} &= \frac{1}{\frac{1}{R_{ri2}} + \frac{1}{R_{ri2}} + \frac{1}{2R_{ri1}+R_{rc}}} \\ &= \frac{(1-\sqrt{S_f})\lambda_c + \sqrt{S_f}\lambda_i}{l_a\lambda_i[(1-\sqrt{S_f}+S_f)\lambda_c + (\sqrt{S_f}-S_f)\lambda_i]} \end{aligned} \tag{10,11}$$

$$\begin{aligned} \lambda_{re} &= \frac{l}{l_a l R_{re}} \\ &= \frac{\lambda_i[(1-\sqrt{S_f}+S_f)\lambda_c + (\sqrt{S_f}-S_f)\lambda_i]}{(1-\sqrt{S_f})\lambda_c + \sqrt{S_f}\lambda_i} \\ &\approx \frac{(1-\sqrt{S_f}+S_f)\lambda_i}{1-\sqrt{S_f}} \end{aligned} \tag{12}$$

$$\begin{aligned} R_{ai1} &= \frac{l_a}{0.5(l-l_c)l_c\lambda_i} \\ R_{ai2} &= \frac{l_a}{0.5(l-l_c)l\lambda_i} \\ R_{ac} &= \frac{l_a}{l_c^2\lambda_c} \end{aligned} \tag{13}$$

$$R_{ae} = \frac{1}{\frac{2}{R_{ai1}} + \frac{2}{R_{ai1}} + \frac{1}{R_{ac}}} = \frac{l_a}{l^2[(1-S_f)\lambda_i + S_f\lambda_c]} \tag{14}$$

$$\lambda_{ae} = \frac{l_a}{l^2 R_{ae}} = (1-S_f)\lambda_i + S_f\lambda_c \tag{15}$$

Nevertheless, the radial and circumferential thermal conductivity of the equivalent thermal model should be equal according to the assumption that the copper wires are uniformly arranged in the slot, which does not agree with the derived results in equations (8) and (12). As a consequence, the topology above will naturally introduce errors, so it is necessary to propose an improved topology.

The improved topology of a single heat conduction unit is shown in FIGURE 5, and the equivalent thermal conductivity in radial and circumferential directions is derived as follows:

$$\begin{aligned} R_{rci1} &= \frac{0.5(l+l_c)}{0.5(l-l_c)l_a\lambda_i} \\ R_{rci2} &= \frac{0.5(l-l_c)}{0.5(l+l_c)l_a\lambda_i} \\ R_{rc} &= \frac{l_c}{l_c l_a \lambda_c} \\ R_{rce} &= 2R_{rci2} + \frac{1}{\frac{1}{R_{rci1}} + \frac{1}{R_{rci1}} + \frac{1}{R_{rcc}}} \\ &= \frac{1}{l_a}\left[\frac{2-2\sqrt{S_f}}{(1+\sqrt{S_f})\lambda_i} + \frac{1+\sqrt{S_f}}{(2-2\sqrt{S_f})\lambda_i + (1+\sqrt{S_f})\lambda_c}\right] \end{aligned} \tag{16,17}$$

$$\begin{aligned} \lambda_{rce} &= \frac{l}{l_a l R_{re}} = \frac{(1+2\sqrt{S_f}+S_f)\lambda_i\lambda_c + (2-2S_f)\lambda_i^2}{(5-6\sqrt{S_f}+5S_f)\lambda_i + (2-2S_f)\lambda_c} \\ &\approx \frac{(1+2\sqrt{S_f}+S_f)\lambda_i}{2-2S_f} \end{aligned} \tag{18}$$

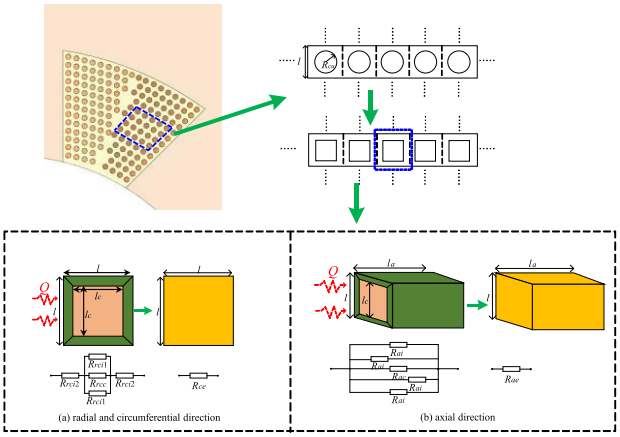


**FIGURE 5.** Improved topology structure of slot-in winding equivalent thermal model.

The equivalent thermal conductivity in axial direction is:

$$R_{ai} = \frac{4l_a}{(l-l_c)(l+l_c)\lambda_i}; \quad R_{ac} = \frac{l_a}{l_c^2\lambda_c} \tag{19}$$

$$R_{ae} = \frac{1}{\frac{4}{R_{ai}} + \frac{1}{R_{ac}}} = \frac{l_a}{l^2[(1-S_f)\lambda_i + S_f\lambda_c]} \tag{20}$$

$$\lambda_{ae} = \frac{l_a}{l^2 R_{ae}} = (1-S_f)\lambda_i + S_f\lambda_c \tag{21}$$

#### 2) END WINDING EQUIVALENT THERMAL MODEL

As the stator winding of RMB is wrapped around the teeth, it could be equivalent to a ring form as shown in FIGURE 6. In this case, the equivalent thermal conductivity in radial, circumferential, and axial directions of the end winding corresponds to the equivalent thermal conductivity in radial, axial, and circumferential directions of the slot-in winding, respectively.

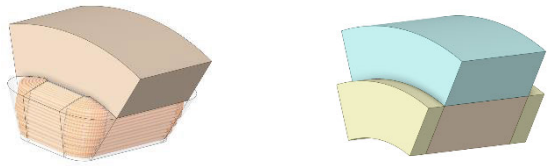


**FIGURE 6.** Equivalent thermal model of end winding.

As to the end winding of the HPMSM, because the hairpin form winding is adopted, which could be approximated to a straight-line segment, the equivalent thermal conductivity of it in different heat transfer directions is the same as slot-in winding.

Above all, for the HPMSM set in this paper, the $S_f$ of the winding in RMB and HPMSM is 0.45 and 0.48 respectively, so the equivalent thermal conductivity of the winding in RMB and HPMSM can be obtained and shown in TABLE 8.

**TABLE 8.** Equivalent thermal conductivity of the winding in RMB and HPMSM.

| Components | | Direction | $\lambda$/W·m$^{-1}$·K$^{-1}$ |
|---|---|---|---|
| RMB | slot-in winding | radial | 0.51 |
| | | circumferential | 0.51 |
| | | axial | 179.21 |
| | end winding | radial | 0.51 |
| | | circumferential | 179.21 |
| | | axial | 0.51 |
| HPMSM machine | slot-in winding | radial | 0.55 |
| | | circumferential | 0.55 |
| | | axial | 191.14 |
| | end winding | radial | 0.55 |
| | | circumferential | 0.55 |
| | | axial | 191.14 |

Based on the conservation of mass, the specific heat capacity $c_p$ and density $\rho$ of the equivalent thermal model of winding in RMB and HPMSM are shown in TABLE 9.

**TABLE 9.** Specific heat capacity and density of winding equivalent thermal model in RMB and HPMSM.

| Components | $c_p$/J·kg$^{-1}$·K$^{-1}$ | $\rho$/kg·m$^{-3}$ |
|---|---|---|
| RMB | 1444.1 | 4687.5 |
| HPMSM | 1387 | 4920 |

#### 3) VERIFICATION WITH FEM AND EXPERIMENT

To verify the accuracy of the proposed equivalent thermal model, the exact model and equivalent model of the winding in RMB is established using FEM. The boundary conditions are set as shown in FIGURE 7, and the thermal contours of them under the same cooling conditions are obtained in FIGURE 8.

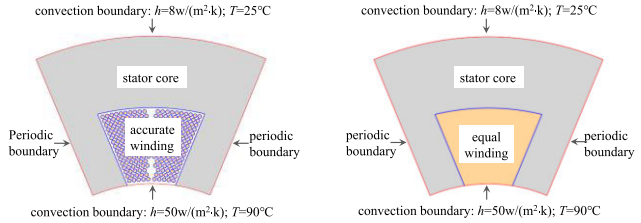


**FIGURE 7.** Accurate model and equivalent model of slot-in winding.

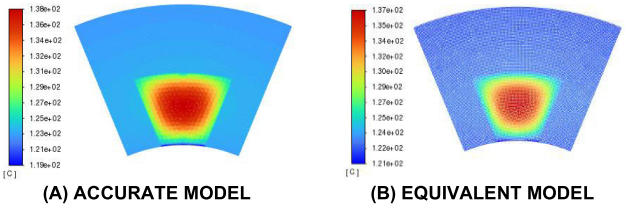


**FIGURE 8.** Comparison of thermal contours.

As shown in FIGURE 8, the high-temperature regions of the exact model and the equivalent model are both located in the middle region of the RMB slot, showing the consistency of spatial distribution characteristics. Moreover, the lowest to highest temperature ranges of the exact model and the equivalent model are 119°C∼138°C and 121°C∼137°C respectively, with a relative difference within 0.7%∼1.7%, which shows that the proposed equivalent thermal model has high precision

The accuracy of the proposed equivalent thermal model was further verified by experiments in [30]. The relative difference between the calculated temperature, which was obtained by using the equivalent thermal model, and the experimental temperature was about 7%.

### B. 3-D LPTN MODEL

#### 1) THERMAL NODES PARTITION

The calculation of LPTN model is based on the heat transfer theory and the thermal network topology. At present, the LPTN model of the machine mainly considers the independent heat transfer in radial and axial directions, but for the typical ''Sandwich'' structure of stator teeth and stator winding, the internal circumferential thermal resistance must be considered. To balance the efficiency and accuracy of calculation, the following settings are made:

(1) Uniformly distributed thermal capacity and heat generation;

(2) Independent heat transfer in radial, circumferential, and axial directions;

(3) Taking a single slot as the basic unit when considering the circumferential thermal resistance, the temperature

between each basic unit is distributed symmetrically along the circumferential direction;

(4) Considering the periodic symmetry of the machine in the circumferential direction, the smallest symmetric unit is taken to establish the LPTN model.

According to the composition of the HPMSM set, it is divided into four sub-models: front RMB, HPMSM, rare RMB, and AMB as shown in FIGURE 9. The specific nodes division of each sub-model and the heat transfer paths between each node are shown in FIGURE 10.

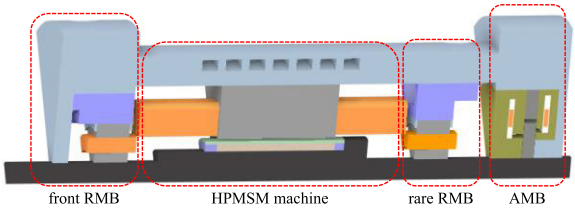


**FIGURE 9.** Division of the HPMSM set.

### 2) THERMAL CONDUCTION RESISTANCE

The key to establishing the LPTN model lies in the calculation of thermal resistance. According to the theory of heat transfer, the thermal resistance for different heat transfer modes is shown in TABLE 10.

**TABLE 10.** Thermal resistance calculation basic equations.

| Modes | Equation | Description |
|---|---|---|
| conduction | $R_{cond}=\frac{L}{kA}$ | $L$ is the length along the direction of heat conduction[m]; $k$ is the thermal conductivity[w/(m·K)]; $A$ is the area perpendicular to the direction of heat transfer[m$^2$] |
| convection | $R_{convt}=\frac{1}{h_cA}$ | $h_c$ is the convective heat transfer coefficient[w/(m$^2$·K)]; $A$ is the heat dissipation area[m$^2$] |
| radiation | $R_{rad}=\frac{1}{h_rA}$ | $h_r$ is the radiant heat transfer coefficient[w/(m$^2$·K)]; $A$ is the heat dissipation area[m$^2$] |

Generally, the effect of heat radiation can be ignored in electric machines, and heat conduction and heat convection are the main forms of heat transfer. According to the periodic symmetry, the key components (i.e. stator winding, stator core, rotor core, etc.) can be equivalent to the basic structure in the form of the hollow cylinder, as shown in FIGURE 11(a). Depending on whether there is a heat source in the component, the classical model or T model can be selected to calculate the thermal conduction resistance, seeing in FIGURE 11(b) and (c). The specific calculation equations are summarized in TABLE 11 [31]. In this paper, the T model is adopted to calculate the thermal conduction resistance of the components with heat sources, such as windings, permanent magnets, etc., and the classical model is adopted to calculate the thermal resistance of the components without heat sources, such as housing, shaft, etc.

**TABLE 11.** Calculation equations of different models.

| Type | Direction | Calculation Equation |
|---|---|---|
| classical model | radial | $R_{r1}=R_{r2}=\frac{\ln(r_2/r_1)}{2\theta Lk_r}$ |
| | circumferential | $R_{c1}=R_{c2}=\frac{\theta}{2k_cL\ln(r_2/r_1)}$ |
| | axial | $R_{a1}=R_{a2}=\frac{L}{\theta k_a(r_2^2-r_1^2)}$ |
| T model | radial | $R_{r1}=\frac{1}{2\theta Lk_r}\left[\frac{2\ln(r_2/r_1)r_2^2}{r_2^2-r_1^2}-1\right]$<br>$R_{r2}=\frac{1}{2\theta Lk_r}\left[1-\frac{2\ln(r_2/r_1)r_1^2}{r_2^2-r_1^2}\right]$<br>$R_{r3}=\frac{-1}{4\theta Lk_r(r_2^2-r_1^2)}\cdot\left[r_2^2+r_1^2-\frac{4r_2^2r_1^2\ln(r_2/r_1)}{r_2^2-r_1^2}\right]$ |
| | circumferential | $R_{c1}=R_{c2}=\frac{\theta}{2Lk_c\ln(r_2/r_1)}$<br>$R_{c3}=-\frac{\theta}{12Lk_c}\left[\frac{3}{\ln(r_2/r_1)}-\frac{r_2^2+r_1^2}{r_2^2-r_1^2}\right]$ |
| | axial | $R_{a1}=R_{a2}=\frac{L}{k_a\theta(r_2^2-r_1^2)}$<br>$R_{a3}=-\frac{L}{3k_a\theta(r_2^2-r_1^2)}$ |

### 3) THERMAL CONVECTION RESISTANCE

The key to calculating the thermal convection resistance is to obtain the CHTC (convection heat transfer coefficient), and researchers have done a lot of work in this area.

The CHTC $h_0$ between the outer surface of the housing and the environment, and the CHTC $h_1$ between the rotating shaft and the internal air can be obtained from the following equation [25]:

$$h_0=14(1+0.5\sqrt{v})\left(\frac{T_{ambient}}{25}\right)^{\frac{1}{3}} \tag{22}$$

$$h_1=15.5(0.39\omega r_{shaft}+1) \tag{23}$$

where $v$ is the velocity of air[m/s], $T_{ambient}$ is the ambient temperature[K], $\omega$ is the speed of machine[rad/s], $r_{shaft}$ is the diameter of the rotating shaft[m].

The CHTC $h_2$ between the inner surface of the housing and internal air, and the CHTC $h_3$ between the rotor end surface, rotor axial ventilation holes and internal air can be calculated by the following equation [32]:

$$h_2=6.5+5.25(\omega r_{rot})^{0.6} \tag{24}$$

$$h_3=16.5(\omega r_{rot})^{0.65} \tag{25}$$

where $r_{rot}$ is the average diameter of rotor[m].

The CHTC $h_4$ between the end winding and internal air can be obtained by the following equation [33]:

$$h_4=41.4(1+0.15v) \tag{26}$$

where $v$ is the velocity of air[m/s].

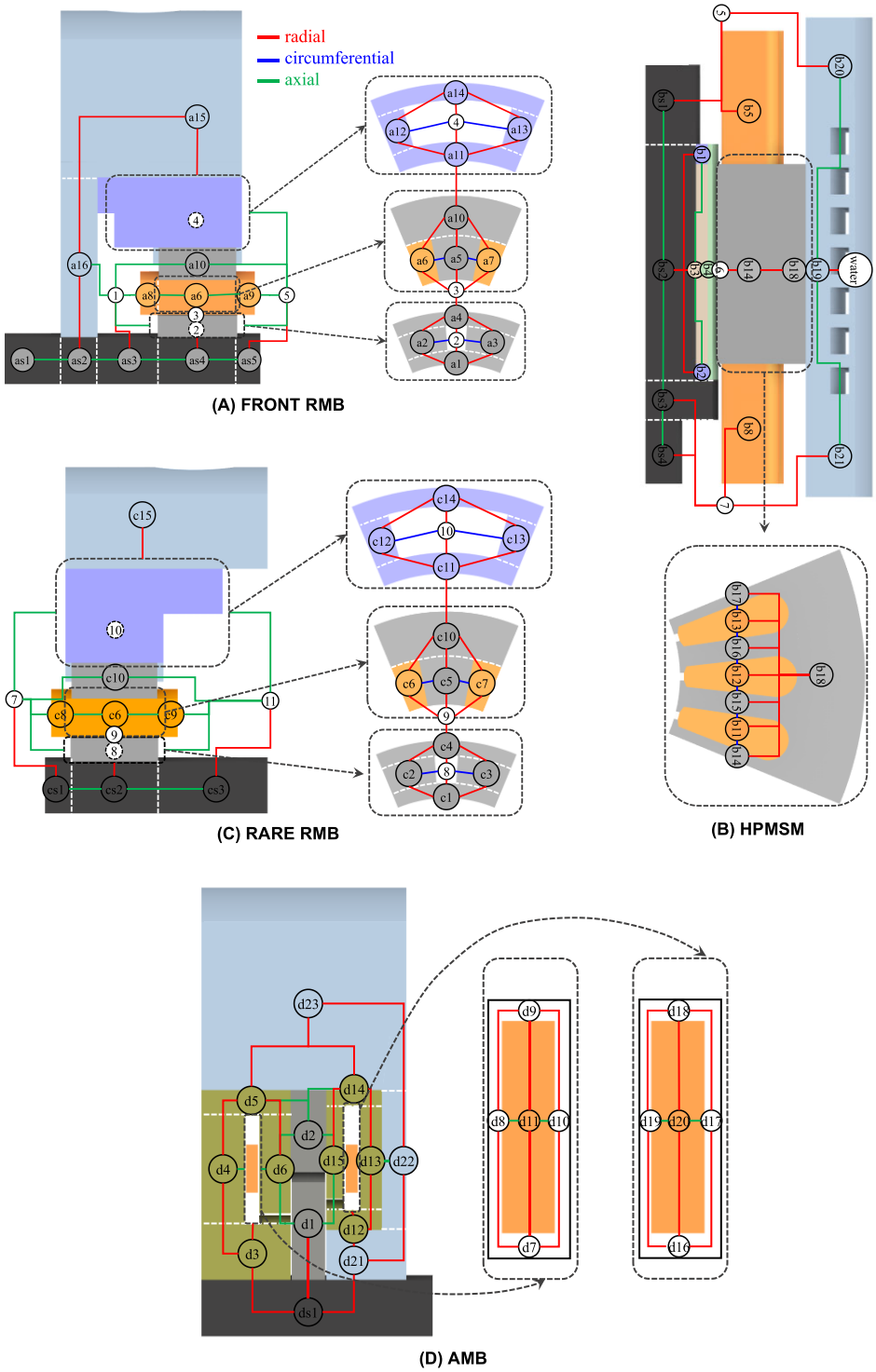


**FIGURE 10.** 3-D LPTN thermal model of the HPMSM set.

The CHTC $h_5$ between the rotor and stator surfaces and air gap can be obtained according to [34]:

$$h_5 = \frac{Nu\lambda_{air}}{\delta} \tag{27}$$

where $\lambda_{\text{air}}$ is the thermal conductivity of air[W/(m·K)], $\delta$ is the length of air gap[m], $Nu$ is Nusselt number, which could be obtained by the following equation:

$$Nu = \begin{cases} 2 & Ta < 1700 \\ 0.128 & Ta^{0.367} 1700 < Ta < 10^4 \\ 0.409 & Ta^{0.241} 10^4 < Ta < 10^7 \end{cases} \tag{28}$$

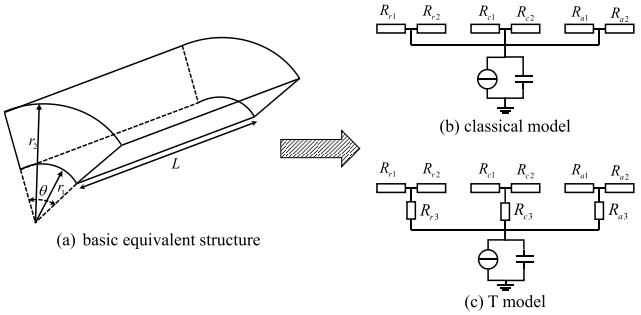


**FIGURE 11.** Thermal conduction resistance models.

where $Ta$ is Taylor number and could be obtained by:

$$Ta = \frac{\mathrm{Re}^2\delta}{r}, \quad \mathrm{Re} = \frac{\rho v\delta}{\mu_{air}} = \frac{\rho\omega r\delta}{\mu_{air}} \tag{29}$$

where $\mu_{\mathrm{air}}$ is the dynamic viscosity of air[kg/(m·s)], $r$ is the diameter of rotor[m].

The Reynolds number of the cooling water in machines generally exceeds 10000, which can be determined as turbulent flow, and the CHTC $h_6$ between the surface of the channel and water can be obtained by [35]:

$$\begin{aligned} h_6 &= \frac{Nu\lambda_{water}}{d_e} \\ Nu &= 0.023\mathrm{Re}^{0.8}\,\mathrm{Pr}^{1/3}\left(\frac{\mu_f}{\mu_w}\right)^{0.14} \\ \mathrm{Re} &= \frac{\rho v d_e}{\mu_{water}} = \frac{\rho v}{\mu_{water}}\cdot\frac{2ab}{a+b} \\ \mathrm{Pr} &= \frac{c_p\mu_{water}}{\lambda_{water}} \end{aligned} \tag{30}$$

(31)

where $\lambda_{water}$ is the thermal conductivity of water[W/m·K], $\rho$ is the density of water[kg/m$^3$], $\mu_{water}$ is the dynamic viscosity of water[kg/(m·s)], $d_e$ is the hydraulic diameter[m], $a$ and $b$ are length and width of water channel respectively[m], $v$ is the velocity of water[m/s], $\mu_f$ and $\mu_w$ are the dynamic viscosity of water under the average temperature and wall temperature respectively[kg/(m·s)].

## IV. THERMAL ANALYSIS AND CFD VERIFICATION

### A. LPTN MODEL CALCULATION

The steady-state thermal equations of the LPTN model can be given in the following form:

$$\boldsymbol{GT} = \boldsymbol{P} \tag{32}$$

where $\boldsymbol{G}$ is the inter-nodal conductance matrix[K/W], $\boldsymbol{T}$ is the nodal steady-state temperature distribution [K], and $\boldsymbol{P}$ is the column vector of nodal power loss[W]. Matrix $\boldsymbol{G}$ is formed by the thermal conductivities of every path as:

$$\boldsymbol{G} = \begin{bmatrix} \sum_{k=1}^{N}\frac{1}{R(k,1)} & -\frac{1}{R(2,1)} & \cdots & -\frac{1}{R(N,1)} \\ -\frac{1}{R(2,1)} & \sum_{k=1}^{N}\frac{1}{R(k,2)} & \cdots & -\frac{1}{R(N,2)} \\ \vdots & \vdots & \vdots & \vdots \\ -\frac{1}{R(N,1)} & -\frac{1}{R(N,2)} & \cdots & \sum_{k=1}^{N}\frac{1}{R(k,N)} \end{bmatrix} \tag{33}$$

where $R$ means the thermal resistance between two nodes, and $N$ means the order of $\boldsymbol{G}$. $\boldsymbol{G}$ and $\boldsymbol{P}$ can be obtained from the previous content.

The transient temperature rises can be expressed by:

$$\frac{d\boldsymbol{T}}{dt} = (\boldsymbol{MC})^{-1}\boldsymbol{P} - (\boldsymbol{MC})^{-1}\boldsymbol{GT} \tag{34}$$

where matrix $\boldsymbol{M}$ is the mass of materials[kg], matrix $\boldsymbol{C}$ is the specific heat [J/(kg·K)]. The analytical solution to the matrix differential equation is derived as [27]:

$$\boldsymbol{T}(t) = e^{\boldsymbol{A}(t-t_0)}\boldsymbol{T}(t_0) + \boldsymbol{A}^{-1}(e^{\boldsymbol{A}(t-t_0)} - \boldsymbol{I})\boldsymbol{B} \tag{35}$$

where $\boldsymbol{I}$ is the unit matrix, $t_0$ is set as 0 in the following analysis, and matrices $\boldsymbol{A}$ and $\boldsymbol{B}$ can be obtained by:

$$\begin{aligned} \boldsymbol{A} &= -(\boldsymbol{MC})^{-1}\boldsymbol{G} \\ \boldsymbol{B} &= (\boldsymbol{MC})^{-1}\boldsymbol{P} \end{aligned} \tag{36}$$

Thus, the transient temperature rises can be obtained.

### B. LPTN RESULTS AND CFD VERIFICATION

#### 1) CFD CALCULATION SETUP

To verify the accuracy of the established LPTN model, CFD method is used to obtain the temperature characteristics of the HPMSM set, and the results of LPTN and CFD are compared with each other. The ambient temperature and cooling water temperature are set at 35°C, which are as same as those in LPTN model. The cooling water flow rate is 20L/min. The loss and material settings are consistent with those mentioned above. To reduce the calculated load, the minimum symmetrical model is also selected for grid division, as shown in Fig. 12, in which the total node number is 359 2908, and orthogonal quality is 0.15.

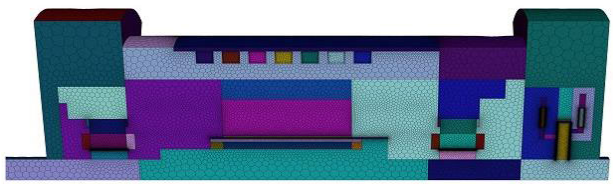

**FIGURE 12.** 3-D meshed model.

### 2) STEADY TEMPERATURE RESULTS

The steady-state temperature results of the HPMSM set under LPTN and CFD models are obtained and shown in FIGURE 13. It can be seen that for the temperature results obtained by LPTN and CFD models, the highest temperature appears in the same component, the rotor PM of the HPMSM. The absolute temperature difference of PM between LPTN model and CFD model is 0.2°C, and the relative temperature difference is 0.16%. In addition to the rotor PM, for other components listed in FIGURE 13 that need to be paid attention to (i.e. stator winding of HPMSM, stator winding of RMB and AMB, rotor of RMB, etc.), the temperature results of LPTN model are in good agreement with them of CFD model. For all these important components, the absolute temperature difference ranges from 0.2 °C to 2.2 °C, and the relative temperature difference ranges from 0.16% to 2%, which verifies the accuracy of the established LPTN model.

### 3) TRANSIENT TEMPERATURE RESULTS

The comparison of the transient temperature results under LPTN model and CFD model is shown in FIGURE 14. Firstly, it can be seen that the trends of the temperature-time curves obtained by LPTN and CFD are completely consistent, and the temperatures of individual components match well at each time point. Specifically, among the temperature results obtained by the LPTN model, the component that best agrees with the CFD temperature results is the rotor of front RMB, in which the absolute temperature difference is less than 1.9°C. and the worst-matched component is the stator teeth of the HPMSM. However, for the worst-matched component of the HPMSM set, the absolute temperature difference at each time step is within 4.1°C during the whole simulation time, and the relative temperature difference is within 4.2%. The transient temperature results further verify the accuracy of the established LPTN model.

The computational efficiency of LPTN model and CFD model is also compared. The LPTN model is run in MATLAB, and the CFD model is run in Fluent. The computing platform is a desktop computer, the processor is i5 9600KF@3.7Ghz, 32G RAM. Record the cost time for MATLAB and Fluent to simulate the same time steps, and compare the calculation time, as shown in TABLE 12.

**TABLE 12. Computational time for LPTN model and CFD model.**

| Model | Calculation Time |
|---|---|
| LPTN | 7.1s |
| CFD | 125.3min |

From the above results, it can be seen that the LPTN model established in this paper has significant advantages in terms of required computing resources, and has quite high computational accuracy.

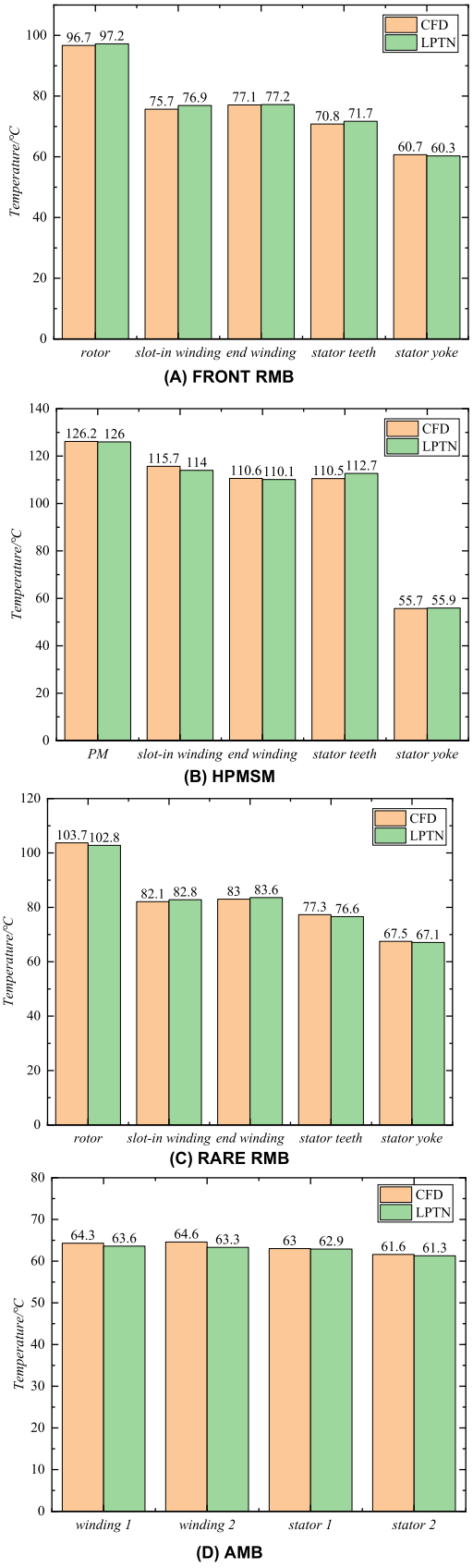


**FIGURE 13. Steady-state temperature results.**

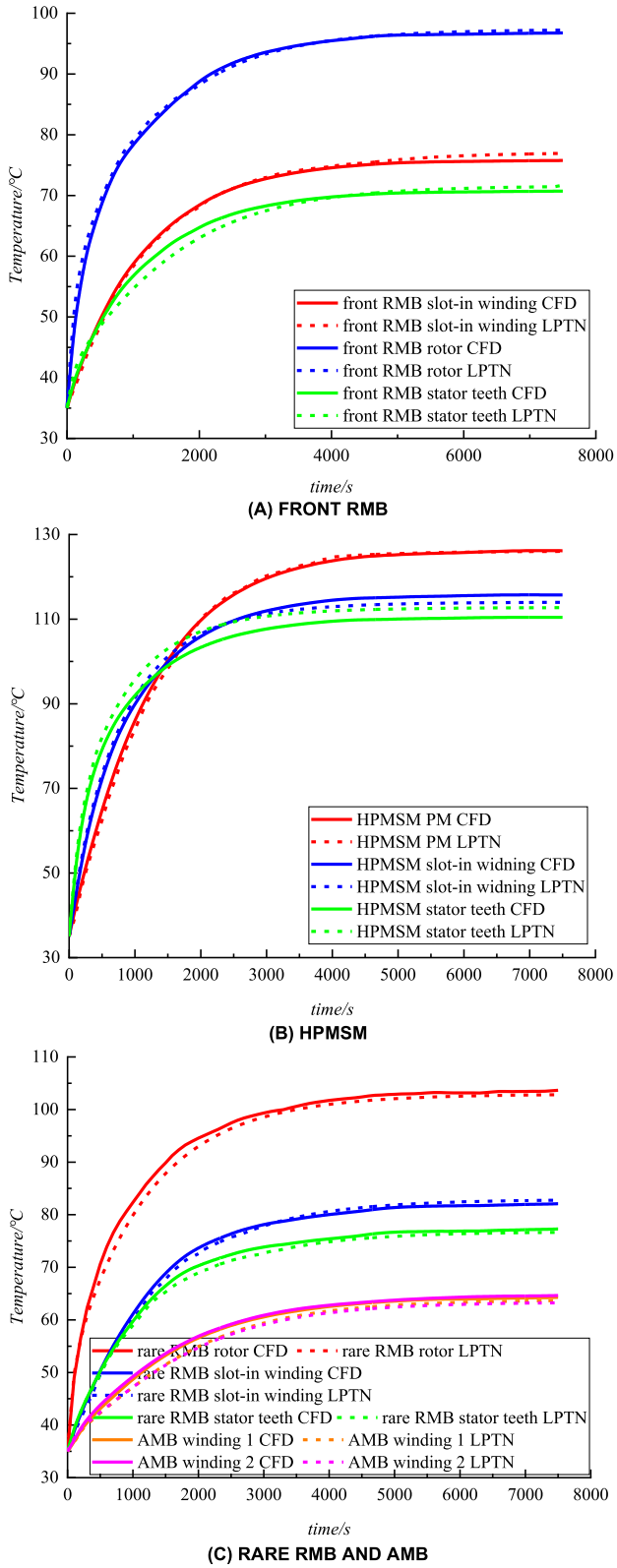


**FIGURE 14.** Transient temperature results.

## V. CONCLUSION

For a 40000rpm HPMSM set, the LPTN model under the coupling state of the machine and magnetic bearings is established in this paper, and its temperature characteristics are analyzed. The following conclusions are obtained:

(1) The equivalent thermal model is derived for the scatter winding. Based on the analysis of the inherent errors of the conventional equivalent thermal model, an improved equivalent topological structure is proposed, and FEM is used to verify it. The results show that the temperature error between the improved equivalent thermal model and the precise thermal model is within 0.7%∼1.7%, and the error with the experimental results is about 7%, which verifies the accuracy of the proposed improved equivalent thermal model.

(2) A 3D LPTN model is established based on the classical heat transfer model and T heat transfer model for the HPMSM set, and the mounted LPTN model under the coupling state of the machine and magnetic bearings is obtained.

(3) The temperature characteristics of key components of the HPMSM set are obtained based on the established LPTN model and compared with CFD model. The results show that the established LPTN model has significant advantages in computing efficiency compared with CFD method, and the results under LPTN model are in good agreement with those under CFD model with a relative difference less than 2% in steady state and 4.2% in transient state respectively, which verifies the accuracy of the proposed LPTN model.

This paper has certain significance for the rapid and accurate analysis of temperature under the coupling state of HPMSM and magnetic bearings, even for temperature prediction. The accuracy of the established LPTN model can be further verified by experiment.

## REFERENCES

[1] S. Rehman, L. M. Alhems, M. M. Alam, L. Wang, and Z. Toor, "A review of energy extraction from wind and ocean: Technologies, merits, efficiencies, and cost," *Ocean Eng.*, vol. 267, Jan. 2023, Art. no. 113192.

[2] M.-J. Li and W.-Q. Tao, "Review of methodologies and polices for evaluation of energy efficiency in high energy-consuming industry," *Appl. Energy*, vol. 187, pp. 203–215, Feb. 2017.

[3] M.-J. Li, H.-H. Zhu, J.-Q. Guo, K. Wang, and W.-Q. Tao, "The development technology and applications of supercritical $CO_2$ power cycle in nuclear energy, solar energy and other energy industries," *Appl. Thermal Eng.*, vol. 126, pp. 255–275, Nov. 2017.

[4] K. Wang, M.-J. Li, J.-Q. Guo, P. Li, and Z.-B. Liu, "A systematic comparison of different S-$CO_2$ Brayton cycle layouts based on multi-objective optimization for applications in solar power tower plants," *Appl. Energy*, vol. 212, pp. 109–121, Feb. 2018.

[5] P. Pan, C. Yuan, Y. Sun, X. Yan, M. Lu, and R. Bucknall, "Thermo-economic analysis and multi-objective optimization of S-$CO_2$ Brayton cycle waste heat recovery system for an ocean-going 9000 TEU container ship," *Energy Convers. Manage.*, vol. 221, Oct. 2020, Art. no. 113077.

[6] X. P. Yan, J. W. Wang, and Y. W. Sun, "Review on s$CO_2$ Brayton cycle power generation technology based on ship waste heat recovery utilization," *China Mech. Eng.*, vol. 30, no. 8, pp. 939–946, 2019.

[7] J. Pasch, T. Conboy, and D. Fleming, "Supercritical $CO_2$ recompression Brayton cycle: Completed assembly description," Tech. Rep., Dec. 2023.

[8] X. Bian, X. Wang, R. Wang, J. Cai, X. Zhang, H. Tian, G. Shu, and L. Shi, "Multimode operation control strategy for improving part-load performance of supercritical $CO_2$ Brayton cycle," *J. Supercritical Fluids*, vol. 200, Sep. 2023, Art. no. 105971.

[9] W. Geng, T. Zhu, Y. Zhang, C. Wu, Y. Wang, Q. Li, and Z. Zhang, "Rotor air-friction loss and thermal analysis of IPM rotors for high speed axial-flux machine," *IEEE Trans. Ind. Appl.*, vol. 59, no. 1, pp. 779–788, Jan. 2023.

[10] Q. Shen, Z. Zhou, S. Li, X. Liao, T. Wang, X. He, and J. Zhang, "Design and analysis of the high-speed permanent magnet motors: A review on the state of the art," *Machines*, vol. 10, no. 7, p. 549, Jul. 2022.
[11] Y. Okada, T. Kosaka, and N. Matsui, "Windage loss reduction for hybrid excitation flux switching motors based on rotor structure design," in *Proc. IEEE Int. Electr. Mach. Drives Conf. (IEMDC)*, May 2017, pp. 1–8.
[12] H. Zuo, Z. Shi, and Y. Zheng, "Loss calculation and thermal analysis of axial AMB in HTR-PM helium circulator," *Appl. Comput.Electromagn. Soc. J.*, vol. 34, no. 4, pp. 591–597, 2019.
[13] Y. Sakurai, T. Matsumura, T. Iida, H. Kanai, N. Katayama, H. Imada, H. Ohsaki, Y. Terao, T. Shimomura, H. Sugai, H. Kataza, R. Yamamoto, and S. Utsunomiya, "Design and thermal characteristics of a 400 mm diameter levitating rotor in a superconducting magnetic bearing operating below at 10 k for a CMB polarization experiment," *IEEE Trans. Appl. Supercond.*, vol. 28, no. 4, pp. 1–4, Jun. 2018.
[14] B. Han, X. Liu, Z. Huang, X. Zhang, and Y. Zhou, "Loss calculation, thermal analysis, and measurement of magnetically suspended PM machine," *IEEE Trans. Ind. Electron.*, vol. 65, no. 6, pp. 4514–4523, Jun. 2018.
[15] G. Du, W. Xu, J. Zhu, and N. Huang, "Power loss and thermal analysis for high-power high-speed permanent magnet machines," *IEEE Trans. Ind. Electron.*, vol. 67, no. 4, pp. 2722–2733, Apr. 2020.
[16] D. L. Liang, S. J. Chu, and S. F. Jia, "Overview of research on key technology of high-temperature and high-speed permanent magnet machine," *J. Xi'An Jiaotong Univ.*, vol. 56, no. 10, pp. 31–48, 2022.
[17] Z. Xu, Y. Xu, W. Liu, and Y. Wang, "Global fluid flow and heat transfer characteristics analysis of an open air-cooled drive motor for drilling application," *Case Stud. Thermal Eng.*, vol. 37, Sep. 2022, Art. no. 102254.
[18] W. Li, Z. Cao, and X. Zhang, "Thermal analysis of the solid rotor permanent magnet synchronous motors with air-cooled hybrid ventilation systems," *IEEE Trans. Ind. Electron.*, vol. 69, no. 2, pp. 1146–1156, Feb. 2022.
[19] R. Burke, A. Giedymin, Z. Wu, H. Chuan, N. Bourne, and J. G. Hawley, "A lumped parameter thermal model for single-sided AFPM machines with experimental validation," *IEEE Trans. Transport. Electrific.*, vol. 6, no. 3, pp. 1065–1083, Sep. 2020.
[20] Y. Ebrahimi and M. R. Feyzi, "Lumped parameter thermal model for axial flux switched reluctance motors," *Electr. Power Compon. Syst.*, vol. 45, no. 20, pp. 2318–2326, Dec. 2017.
[21] J. Yang and Z. Wang, "A simple and accurate method for estimating the stator winding real-time temperature of air-cooled hydrogenerator," *Thermal Sci.*, vol. 27, no. 1, pp. 167–177, 2023.
[22] Z. Sheng, D. Wang, J. Fu, and J. Hu, "A computationally efficient spatial online temperature prediction method for PM machines," *IEEE Trans. Ind. Electron.*, vol. 69, no. 11, pp. 10904–10914, Nov. 2022.
[23] X. Liu, H. Yu, Z. Shi, L. Huang, T. Xia, and R. Guo, "Porous metal model for calculating slot thermal conductivity coefficient of electric machines," *Appl. Thermal Eng.*, vol. 111, pp. 981–988, Jan. 2017.
[24] S. Nategh, O. Wallmark, M. Leksell, and S. Zhao, "Thermal analysis of a PMaSRM using partial FEA and lumped parameter modeling," *IEEE Trans. Energy Convers.*, vol. 27, no. 2, pp. 477–488, Jun. 2012.
[25] Q. Chen, D. Liang, L. Gao, Q. Wang, and Y. Liu, "Hierarchical thermal network analysis of axial-flux permanent-magnet synchronous machine for electric motorcycle," *IET Electr. Power Appl.*, vol. 12, no. 6, pp. 859–866, Jul. 2018.
[26] G. Bertotti, "General properties of power losses in soft ferromagnetic materials," *IEEE Trans. Magn.*, vol. 24, no. 1, pp. 621–630, Jan. 1988.
[27] W. Yu, W. Hua, J. Qi, H. Zhang, G. Zhang, H. Xiao, S. Xu, and G. Ma, "Coupled magnetic field-thermal network analysis of modular-spoke-type permanent-magnet machine for electric motorcycle," *IEEE Trans. Energy Convers.*, vol. 36, no. 1, pp. 120–130, Mar. 2021.
[28] J. Saari, *Thermal Analysis High-Speed Induction Machines*. Helsinki University of Technology, 1998.
[29] Y. Tang, S. Sun, W. Yu, and W. Hua, "Thermal analysis of water-cooling permanent magnet synchronous machine for port traction electric vehicle," *Electronics*, vol. 12, no. 3, p. 734, Feb. 2023.
[30] B. Liu, Z. J. Yu, and J. Fu, "Cooling design and temperature field analysis of radial-axial magnetic bearings," in *Proc. CSEE*, 2023, pp. 1–12.
[31] Z. Y. Sheng, *Research on the Online Thermal Model and Its Application for PM Electrical Machine*. Southeast Univ., 2023.
[32] G. D. Demetriades, H. Z. de la Parra, E. Andersson, and H. Olsson, "A real-time thermal model of a permanent-magnet synchronous motor," *IEEE Trans. Power Electron.*, vol. 25, no. 2, pp. 463–474, Feb. 2010.
[33] A. Boglietti and A. Cavagnino, "Analysis of the endwinding cooling effects in TEFC induction motors," *IEEE Trans. Ind. Appl.*, vol. 43, no. 5, pp. 1214–1222, May 2007.
[34] S. Wahsh, J. Shazly, and A. Yassin, "Steady state heat conduction problems of AFPMSM using 3D finite element," in *Proc. 18th Int. Middle East Power Syst. Conf. (MEPCON)*, Dec. 2016, pp. 949–953.
[35] Q. Lu, X. Zhang, Y. Chen, X. Huang, Y. Ye, and Z. Q. Zhu, "Modeling and investigation of thermal characteristics of a water-cooled permanent-magnet linear motor," *IEEE Trans. Ind. Appl.*, vol. 51, no. 3, pp. 2086–2096, May 2015.
[36] J. Pyrhonen, T. Jokinen, and V. Harbovcova, *Design of Rotating Electrical Machines*. Hoboken, NJ, USA: Wiley, 2013.

**LIU BIN** received the B.S. degree in aircraft design and engineering from Beihang University, Beijing, China, in 2019, and the M.S. degree in electrical engineering from the Naval University of Engineering, Wuhan, China, in 2021, where he is currently pursuing the Ph.D. degree in electrical engineering.

**YU ZHONGJUN** received the Ph.D. degree in aircraft design and engineering from Beihang University, Beijing, China, in 2009.

Since 2009, he has been an Associate Professor and a Professor with the National Key Laboratory of Electromagnetic Energy, Naval University of Engineering. His research interests include electric propulsion and efficient cooling technology.

**FU JIA** received the Ph.D. degree in mechanics from the National University of Defense Technology, Changsha, China, in 2017.

Since 2017, he has been an Associate Professor with the National Key Laboratory of Electromagnetic Energy, Naval University of Engineering. His research interests include high-power machine design and efficient cooling technology.